

ARTICLE

DOI: 10.1038/s41467-018-03169-0

OPEN

Surface passivation engineering strategy to fully-inorganic cubic CsPbI₃ perovskites for high-performance solar cells

Bo Li¹, Yanan Zhang¹, Lin Fu¹, Tong Yu¹, Shujie Zhou¹, Luyuan Zhang¹ & Longwei Yin¹

Owing to inevitable thermal/moisture instability for organic-inorganic hybrid perovskites, pure inorganic perovskite cesium lead halides with both inherent stability and prominent photovoltaic performance have become research hotspots as a promising candidate for commercial perovskite solar cells. However, it is still a serious challenge to synthesize desired cubic cesium lead iodides (CsPbI₃) with superior photovoltaic performance for its thermodynamically metastable characteristics. Herein, polymer poly-vinylpyrrolidone (PVP)-induced surface passivation engineering is reported to synthesize extra-long-term stable cubic CsPbI₃. It is revealed that acylamino groups of PVP induce electron cloud density enhancement on the surface of CsPbI₃, thus lowering surface energy, conducive to stabilize cubic CsPbI₃ even in micrometer scale. The cubic-CsPbI₃ PSCs exhibit extra-long carrier diffusion length (over 1.5 μm), highest power conversion efficiency of 10.74% and excellent thermal/moisture stability. This result provides important progress towards understanding of phase stability in realization of large-scale preparations of efficient and stable inorganic PSCs.

¹Key Laboratory for Liquid-Solid Structural Evolution and Processing of Materials, Ministry of Education, School of Materials Science and Engineering, Shandong University, Jinan 250061, P. R. China. Correspondence and requests for materials should be addressed to L.Y. (email: yinlw@sdu.edu.cn)

Due to suitable direct bandgap, high absorption coefficient, and extra-long carrier diffusion length, excellent optoelectronic property, simple and reproducible solution/vapor-chemistry processing^{1–3}, organic–inorganic hybrid halide perovskite materials (ABX_3 , $\text{A}=\text{CH}_3\text{NH}_3$, $\text{B}=\text{Pb}$, $\text{X}=\text{Br}$, I) have been deemed as a promising candidate for light harvester for next-generation high-performance solar cells^{4–8}. Despite great progress in photovoltaic performance in the last few years, commercial application of perovskite solar cell (PSC) still suffers from moisture and thermal instability owing to the degradation and volatilization of organic component, which presents the uppermost obstacle in further development and mass production⁹. For this reason, all inorganic halide perovskite formed by substituting the organic cation with cesium (Cs) is an optimal alternative for its native inorganic structure stability, and has demonstrated equally efficient and more stable compared to organic–inorganic halide perovskites^{10–13}.

Of the various inorganic lead halide perovskites, especially, cesium lead iodide (CsPbI_3) in cubic phase (α phase) with a bandgap of around 1.73 eV and a visible-light-absorption spectrum up to 700 nm is the mostly desired light harvester in solar cells^{14–16}. However, cubic CsPbI_3 can only keep stable at high temperature of above 300 °C¹⁴. As temperature decreasing to ambient temperature, CsPbI_3 suffers from thermodynamically phase transition to undesired orthorhombic phase (δ phase) with a wide bandgap of 2.82 eV (Supplementary Figure 1), exhibiting an extremely poor photovoltaic conversion efficiency (PCE) of only 0.09% in PSC¹⁷. To overcome this obstacle, composition engineering which pursues a certain amount of bromide (Br) to substitute iodide (I) can be one of efficient methods by balancing the tolerance coefficient between PbX_6 octahedron and Cs ions^{18–20}. For example, Sutton et al.¹⁸ developed a full set of cesium lead halide films from CsPbBr_3 to CsPbI_3 , demonstrating a stabilized power output of 5.6% and J - V efficiency reaching 9.8% for PSC based on cubic CsPbI_2Br , although CsPbI_2Br still reverts to δ phase over prolonged exposure in air. Increasing continuously bromide proportion induces more prominent phase stability/moisture-stability, dispiritingly, which brings Br-widened bandgap near or above 2.0 eV compared with the ideal solar spectrum (from 1.1 eV to 1.7 eV)²¹. Another effectual method to stabilize cubic phase CsPbI_3 is synthesizing colloidal quantum dots (CQDs) with well-controlled size via hot injection process, and best-performance CsPbI_3 solar cells are achieved by assembling cubic phase CsPbI_3 CQDs as photoactive layer^{22–25}. Unfortunately, the undesired α -to- δ phase transition of Cs-based inorganic perovskite has not been inhibited in the solution-chemistry processed film. It is of great and fundamental challenge to develop effective and facile route to synthesize cubic Cs-based inorganic perovskite film for high-performance PSC for potential large-scale industrial application.

Herein, poly-vinylpyrrolidone (PVP)-induced surface passivation strategy is reported to stabilize inorganic perovskite CsPbI_3 with cubic crystal structure via a reproducible solution-chemistry reaction process. The surface chemical state of cubic CsPbI_3 crystals synthesized in the presence of PVP is investigated via Fourier transformed infrared (FTIR) and nuclear magnetic resonance (NMR) techniques, demonstrating that decreased surface tension can be conducive to stabilize cubic CsPbI_3 even in large scale of film with micrometer scale, due to enhanced electron cloud density on the surface of CsPbI_3 originated from chemical bonding between acylamino group in PVP and CsPbI_3 . The obtained cubic CsPbI_3 exhibits extra-long carrier lifetime of 338.7 ns and diffusion length of greater than 1.5 μm , up to an order of magnitude compared to the active layer depth. The fabricated PSCs based cubic CsPbI_3 achieves the highest power conversion efficiency of 10.74% and excellent thermal/moisture stability.

Results

VVP-induced cubic phase stability studies. The specific cubic-phase CsPbI_3 films were prepared via a simple and reproducible one-pot solution spin-coating process using a mixture of CsI, PbI_2 , and PVP as a precursor. X-ray diffraction (XRD) patterns of the CsPbI_3 films coated on the F-doped SnO_2 (FTO) substrates present the difference in the presence and absence of PVP. In the one-pot solution process without PVP, the CsPbI_3 film exhibits a prompt transition from cubic phase to orthorhombic phase when prolonging anneal time or cooling to room temperature, as shown in the XRD pattern (black line) in Fig. 1a and the photograph in Fig. 1b. After adding PVP and gradually increasing the concentration to 10 wt%, the CsPbI_3 can keep stable cubic phase both at high and room temperature, even stable at exceeding 80 days (Fig. 1a, b; Supplementary Fig. 2). Similarly, the prominent phase stability is demonstrated achievable in full series of inorganic perovskite compositions from CsPbI_3 to CsPbBr_3 shown in Supplementary Figures 3 and 4.

We further fabricate CsPbI_3 film on mesoporous TiO_2 via one-step solution spin-coating process with different PVP concentrations. As shown in SEM images of Fig. 1c, d, both orthorhombic and cubic CsPbI_3 exhibit high-surface coverage. Compared with irregular grain size distribution of orthorhombic ones, the obtained PVP-induced cubic CsPbI_3 film presents a dense grained uniform morphology with comparatively small grain size of around 100 nm. The cross-section morphology of the fabricated solar device architecture is shown in Fig. 1e, consisting mainly of two uniform layers containing a 400 nm mesoporous $\text{TiO}_2/\text{CsPbI}_3$ nanocomposite film and a 100 nm pure CsPbI_3 perovskite overlayer. It is shown that the inorganic perovskite materials are fully permeated into TiO_2 mesoporous layer, forming a very uniform overlayer with 100% coverage. Intriguingly, tuning anneal time range, the spin-coating obtained CsPbI_3 exhibits crystalline size of over 1 μm and high-crystalline with cubic phase structure (Supplementary Figs. 5, 6 and 7), which is different from the previous reports involving of phase transition of perovskite materials in large grain size²².

In order to gain insight into the PVP stabilization mechanism on cubic CsPbI_3 , we examine the infrared transmittance spectra of CsPbI_3 films (Fig. 2a) for pure PVP, CsPbI_3 film synthesized in the presence of PVP, and the CsPbI_3 film after removing PVP washed with isopropanol (IPA). The IR spectrum of pure PVP shows absorption bands in the region of 1668, 1421, and 1297 cm^{-1} , which are attributed to typically functional groups of C=O, C–H, and C–N stretching vibration in acylamino of PVP, respectively^{26,27}. For the IR spectrum of the CsPbI_3 film synthesized in the presence of PVP, these characteristic vibrations are still persisted, but only blue-shifting to 1652 cm^{-1} for the C=O stretching, and 1282 cm^{-1} for the C–N stretching, respectively, indicating an interaction effect between functional groups of PVP and precursor ions of CsPbI_3 . For the CsPbI_3 film washed with IPA, characteristic bands for C=O, C–N, and C–H stretching decreases considerably in terms of intensity, while it remains at the same location. A similar binding energy variation of CsPbI_3 surface elements can be found in X-ray photoelectron spectroscopy (XPS) measurements in Supplementary Figure 9. The variation tendency demonstrates that PVP is not only absorbed on the surface of CsPbI_3 physically, but also functions chemically in formation and stabilization of cubic CsPbI_3 through N–C=O bond of acylamino group²⁷.

On the basis of the above IR information, it is indicated that acylamino group of PVP plays a dominant role on the nucleation and growth of cubic CsPbI_3 perovskite film. For further understanding this specific effect of acylamino group of PVP, the liquid-state $^1\text{H}/^{13}\text{C}$ NMR measurement is conducted on pure PVP samples and CsPbI_3 perovskite synthesized in the presence

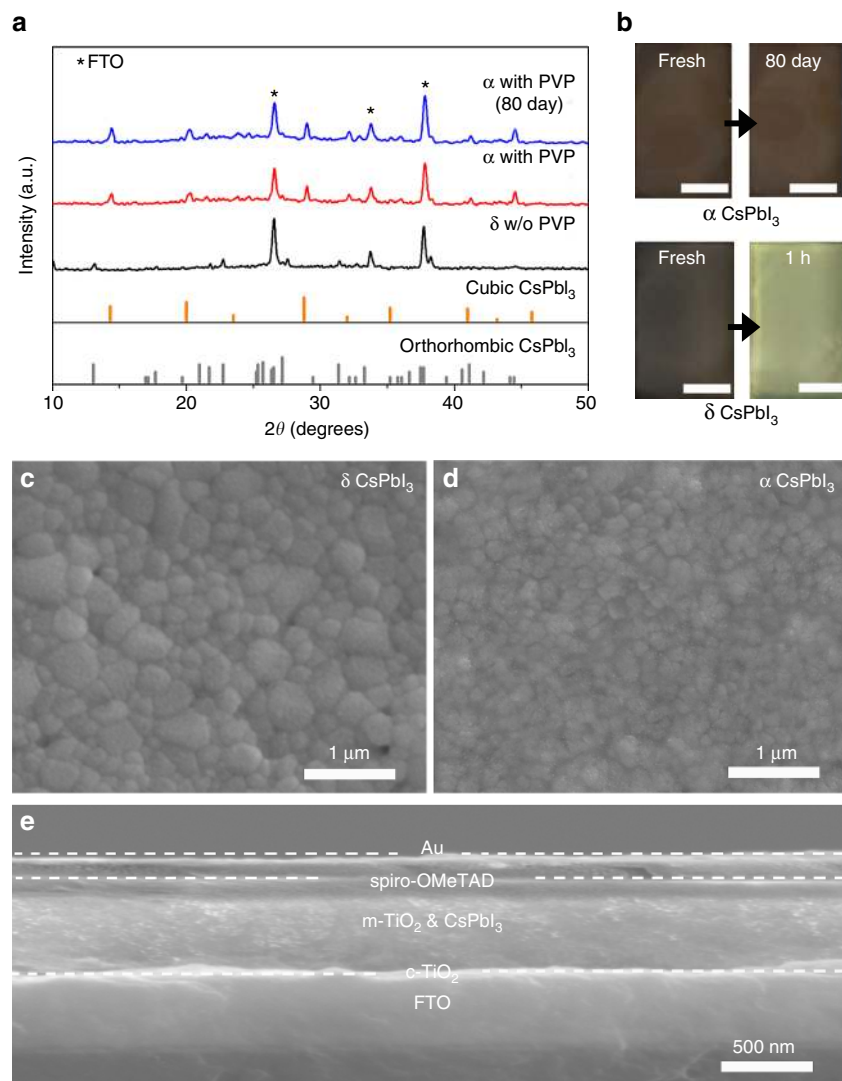


Fig. 1 Structure and morphology of CsPbI_3 films and CsPbI_3 perovskite solar cell. **a** X-ray diffraction (XRD) spectra of CsPbI_3 with orthorhombic phase (δ , black line), cubic phase (α , red line) and stable cubic phase aging 80 days (blue line). The reference powder pattern for CsPbI_3 (cubic and orthorhombic phase) is from Swarnkar et al.²⁵ **b** Images of prepared orthorhombic and cubic CsPbI_3 films aging for different times. Scale bar, 1 cm. **c**, **d** Scanning electron microscope (SEM) images of the overlayers for orthorhombic and cubic CsPbI_3 films deposited on the meso-TiO₂ annealing for 5 min at 300 °C. **e** The typical cross-section SEM image of fabricated inorganic perovskite CsPbI_3 solar cell

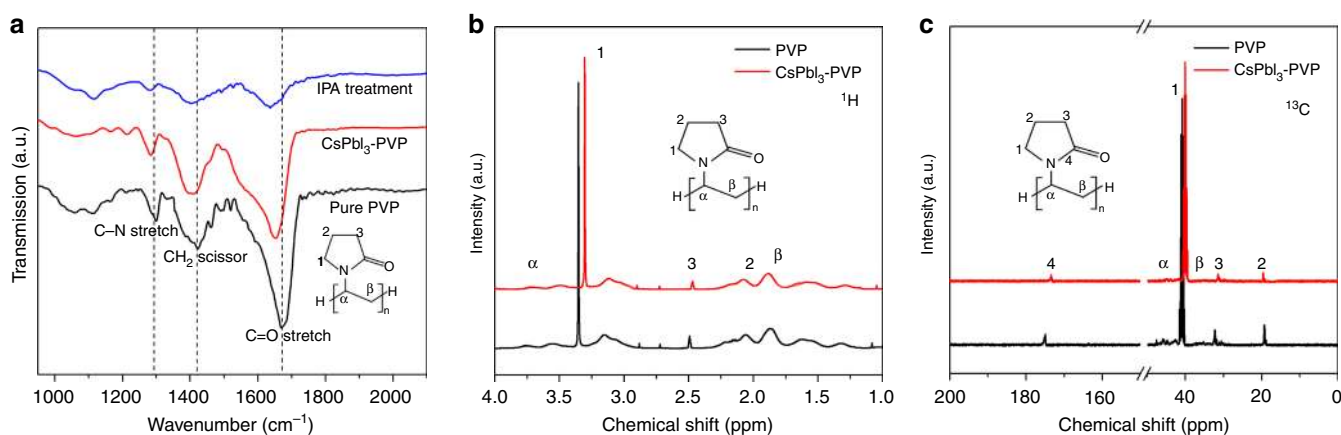


Fig. 2 Fourier transform infrared and nuclear magnetic resonance spectra of CsPbI_3 . **a** Fourier transform infrared (FTIR) spectroscopy of pure PVP, cubic phase CsPbI_3 films synthesized in the presence of PVP, and cubic CsPbI_3 films after IPA treatment. **b**, **c** ¹H and ¹³C liquid-state nuclear magnetic resonance (NMR) spectra of PVP solution and CsPbI_3 perovskite solution in the presence of PVP dissolved with DMSO-d₆

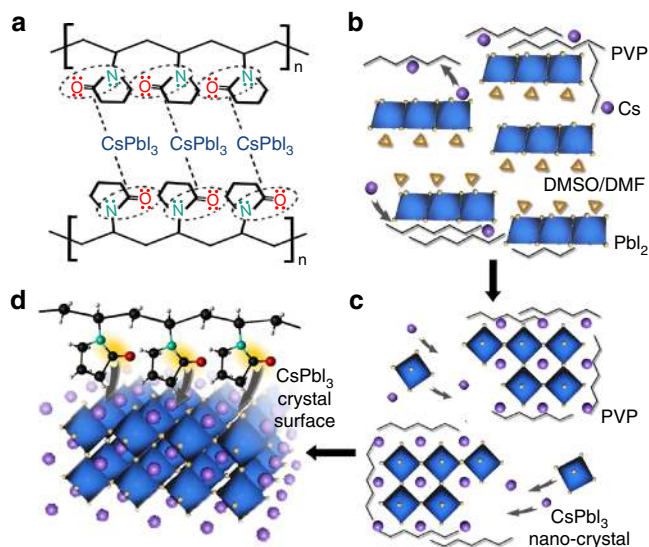


Fig. 3 Mechanism of PVP-induced cubic phase stability. **a** Schematic diagram of the chemical bonding between CsPbI₃ and PVP molecules. PVP molecule contains of long-chain alkyls and acylaminos. The unbounded lone pairs for N/O atoms in acylaminos offer excess electrons and interact with Cs ions in CsPbI₃. Mechanism and scheme for the formation of cubic phase CsPbI₃ with the assistant of PVP in three stages. **b** Pbl₂ and Cs ions in DMF/DMSO solvent assemble and interact with PVP molecules spontaneously, and maintain a metastable state. **c** CsPbI₃ nanocrystals formed attached on PVP molecules, and remain relatively independent and stable under the effect of PVP molecules. **d** PVP anchored at the surface of CsPbI₃ crystals via the combination between N/O and Cs. The negative state in CsPbI₃ crystals surface reduces surface tension significantly and stabilizes cubic phase

of PVP in deuterated DMSO-d₆ solution, as shown in Fig. 2b, c. In ¹H NMR spectra (Fig. 2b) of neat PVP sample, resonance signals attributed to the acylamino group appear at $\delta = 2.5$ and 3.35 ppm, which are characteristic of CH₂ attached to C=O group and N atom, respectively²⁸. The interaction of unique groups in PVP with precursor ions of CsPbI₃ induces a downfield chemical shift of $\Delta\delta \approx 0.5$ ppm for CH₂ adjoining with acylamino group. Reversely, almost no variation for the resonances of hydrogen in backbone chain appears. This can be rationally explained in terms of strengthening effects of resonance for organic constituents through the interaction between cesium cations of perovskite and atoms in organic molecules of PVP, reflecting on the shift of chemical resonances²⁹. Moreover, the result indicates that the N and O atoms in acylamino group are jointly responsible for the chemical shift and can be as two possible centers for coordination with cesium ions. Furthermore, ¹³C NMR spectroscopy in Fig. 2c show that resonance signal of $\delta = 175$ ppm arising from C=O group undergoes a significant downfield shift of $\Delta\delta \approx 2$ ppm on interaction of PVP with CsPbI₃, which is indicative of the coordination-bonding interaction between oxygen atoms of acylamino group and cesium ions in perovskite³⁰. In contrast, the resonances at $\delta = 41$ and 43 ppm for C(1)H₂ and C(α)H attached to nitrogen atoms exhibit slight chemical shift. Such variation of PVP molecule structure further confirms that there exist two potential centers, i.e. the nitrogen and the carbonyl oxygen, interacting with Cs⁺ ions of perovskite exposed³¹. Moreover, the oxygen in acylamino group occupies a dominate position in the formation of C=O...Cs bonds, since nitrogen in planar conformation of internal amide can only have relatively weak influence.

A conceivable PVP-induced surface tension-driven mechanism for the formation of stable cubic phase CsPbI₃ is proposed based

on the above experiment facts. It is known that the acylamino group in N-vinylpyrrolidone molecule of PVP has donated lone pairs related to oxygen and nitrogen atoms, which offer a large number of coordination centers. As shown in Fig. 3a, the coordination modus indicates the polymer molecules coordinate onto the surface of CsPbI₃ through the oxygen atoms, to a lesser extent, via the nitrogen of N-C=O groups, resulting in a weakening of the C=O bonding and an increasing of N-C bond. At the initial stage (Fig. 3b), PVP molecules initiate to attract cations of CsPbI₃ precursors due to long backbone chain and electronegative acylamino group structure. The positive and negative ions of CsPbI₃ tend to assemble and bond to form cubic CsPbI₃ a metastable state around the N-C=O coordination centers of PVP. With time increasing, more nuclei of CsPbI₃ are promptly launched with PVP attached. The PVP molecules, in the meantime, stabilize the CsPbI₃ nanocrystals from aggregation owing to the intermolecular rejection effect, as shown in Fig. 3c. For the grown CsPbI₃ nanocrystals, long-chain PVP molecules with a large number of acylamino groups anchored at the surface of CsPbI₃ provide more coordination polymer units for interactions between oxygen, nitrogen in acylamino and cesium ions of inorganic perovskite. With the growth of CsPbI₃ stabilized with PVP, the interactions between N-C=O of acylamino and Cs⁺ of inorganic perovskite exposed at the surface are enhanced, contributing increasing negative field in Cs⁺-PVP complex on the surface of CsPbI₃ (Fig. 3d), which results in the enhancement of the electron cloud for Cs⁺ of CsPbI₃^{26,32}. According to study by Grätzel's group that the surface free energy is a function of the surface tension³³. While the surface tension is related to charge density³⁴. An increase in charge density decreases the surface tension. Therefore, in the CsPbI₃-PVP complex, the increase in the electron cloud density may result in low surface tension, thus greatly reduces the surface energy of CsPbI₃. As a result, the cubic CsPbI₃ can be maintained at ambient temperature. Furthermore, cubic structure of CsPbI₃ can even be still maintained after 80 days for the PVP chemically functionalized CsPbI₃. Owing to the increase of surface charge originated from the interaction between PVP and CsPbI₃, the surface tension of CsPbI₃ grains reduced significantly, which plays an essential role in the stabilization of cubic phase CsPbI₃.

Optical and photovoltaic performance. Weighing the phase stability and power conversion efficiency (Supplementary Figs. 8, 14, 15 and 16), the optimal synthetic condition (10 wt% of PVP, 5 min annealing, and 30 min IPA treatment) was selected and applied for the following optical, electrical and photovoltaic investigation. Figure 4a presents the ultraviolet-visible absorption spectra of the obtained cubic and orthorhombic phase CsPbI₃ films. The orthorhombic CsPbI₃ exhibits limited visible-light-absorption range less than 450 nm, demonstrating that it is unsatisfactory as an optical active material for solar devices. Oppositely, the cubic CsPbI₃ shows a desired absorption width to 700 nm, nearly covering full visible-light region. Furthermore, we investigate the effect of anneal time (crystalline grains) on the optical properties and carry out the PL measurement of cubic CsPbI₃ perovskite films. The result shows that, tuning size of cubic CsPbI₃ grains, the emission peaks red-shift gradually until to a constant value of around 710 nm (Supplementary Fig. 10).

The time-resolved photoluminescence (TRPL) measurement (Fig. 4b; Supplementary Figure 18) is conducted to investigate the carrier lifetime of cubic and orthorhombic CsPbI₃ films. To eliminate the effect of quenching treatment, the CsPbI₃ films are deposited on glass slides under the same solution-method and the same thickness. The corresponding steady-state PL spectra of cubic and orthorhombic CsPbI₃ films are shown in

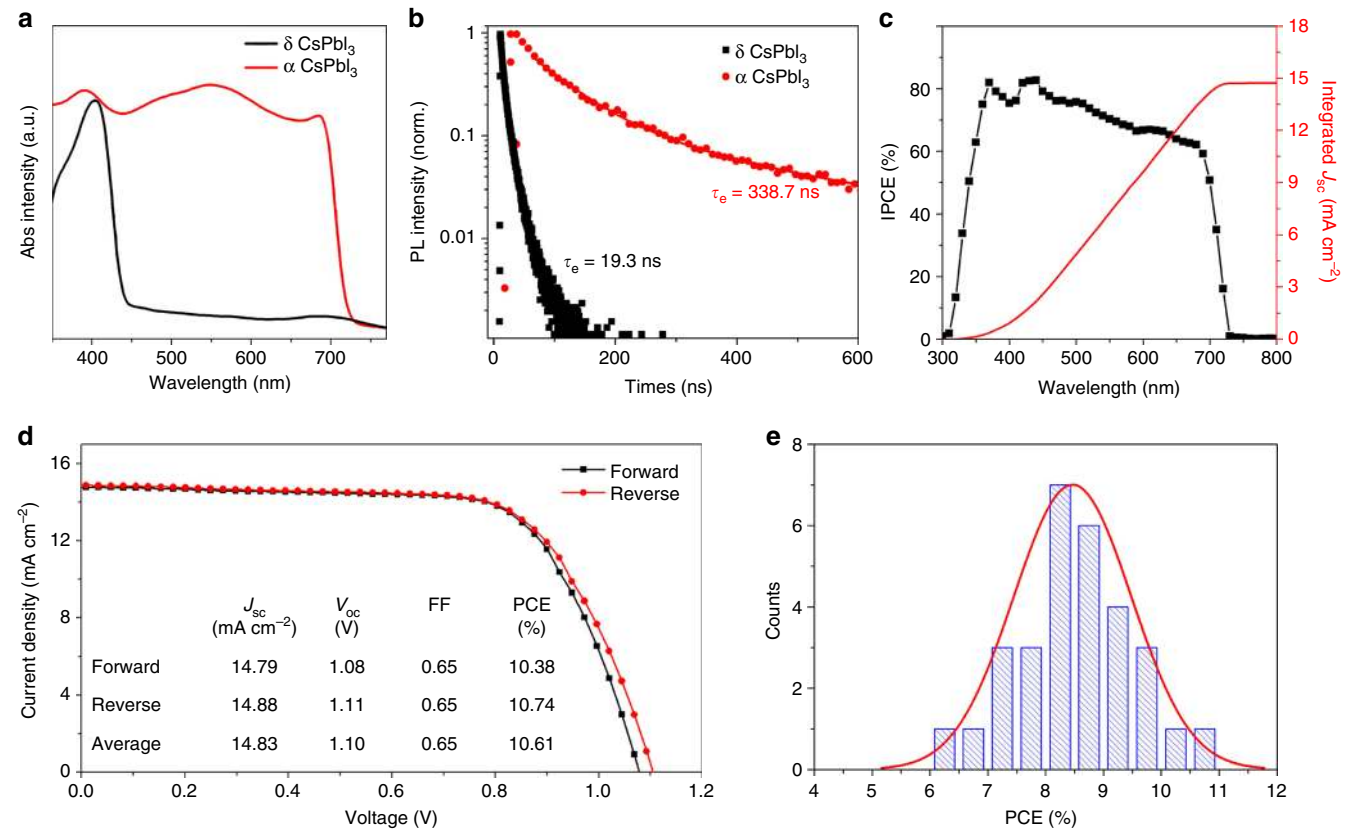


Fig. 4 Optical and photovoltaic performance of cubic CsPbI₃. **a** The ultraviolet-visible (UV) absorption spectra of orthorhombic and cubic CsPbI₃ films. **b** Time-resolved photoluminescence (TRPL) spectra of orthorhombic and cubic CsPbI₃ films deposited on glass substrates. The excitation wavelength was fixed at 300 nm, the emission wavelengths were set at 412 and 704 nm for orthorhombic and cubic, respectively. **c** The incident photon-to-current efficiency (IPCE) spectrum and corresponding integrated J_{sc} for the best-performance cubic CsPbI₃ solar cell. **d** The J - V curves for the best cubic CsPbI₃ cell measured by forward and reverse scans. The average photovoltaic performance values from the two J - V curves are summarized (inset). **e** Histogram of average efficiencies for 30 devices of cubic CsPbI₃.

Supplementary Figure 11. The PL decay for neat orthorhombic CsPbI₃ film exhibits a time-constant of $\tau_e = 19.3$ ns. In contrast, cubic CsPbI₃ film shows an extra-long carrier lifetime of $\tau_e = 338.7$ ns. To simulate the carrier diffusion length in perovskite films, only electron/hole extraction layers and inorganic perovskite layer (i.e., TiO₂/CsPbI₃ and CsPbI₃/spiro-OMeTAD) are fabricated via same solution-chemistry processing and the same thickness with the fabricated cell, the PL decay curves with electron/hole extraction layers are shown in Supplementary Figures 12 and 13, the PL decay dynamics are modeled via accounting the excitations number and distributions based on the one-dimensional diffusion equation¹.

$$\frac{\partial n(x,t)}{\partial t} = D \frac{\partial^2 n(x,t)}{\partial x^2} - k(t)n(x,t) \quad (1)$$

in which $n(x,t)$ is the number of excitations within a certain thickness of perovskite film, $k(t)$ is the PL decay rate without quenching layer, and D is the diffusion coefficient. Table 1 shows the carrier diffusion length for both orthorhombic and cubic CsPbI₃ films, which depends on electron or hole quenching layer used, and it is assumed that all photogenerated carriers reach the quenching interface. It is clear the diffusion length of both electron and hole in orthorhombic CsPbI₃ film is around 120 nm. However, for cubic CsPbI₃ film, the carriers exhibit a diffusion length for electrons over 1 μ m, and even over 1.5 μ m. As reported (Supplementary Table 1), the average carrier diffusion length in organic-inorganic hybrid perovskites MAPbI₃ and FAPbI₃ is 129

Table 1 The carrier diffusion constant (D) and diffusion length (L_D) simulated from PL decays using the diffusion model

Phase	Species	D (cm ² s ⁻¹)	L_D (nm)
Cubic	Electrons	0.061 ± 0.016	1566 ± 254
	Holes	0.057 ± 0.013	1427 ± 238
Orthorhombic	Electrons	0.014 ± 0.009	121 ± 51
	Holes	0.011 ± 0.007	117 ± 35

The errors arise predominantly from perovskite film thickness variations, which is ± 50 nm for both orthorhombic and cubic CsPbI₃ films

and 813 nm, respectively^{1,8}. In addition, in pure/mixed Br based inorganic perovskite, the carrier diffusion length is less than 200 nm¹². The ultra-long carrier diffusion length not only originates from the excellent carrier transport capability of cubic CsPbI₃, but also from the inhibition of defect recombination via the surface passivation effect, which provides the feasibility in planar-structure PSCs or even thicker light-absorption layers.

On the basis of optical and carrier transport properties, we conduct the photovoltaic measurements of the cubic CsPbI₃ PSCs fabricated with mesoporous TiO₂ scaffold. Of the solar devices acquired, Fig. 4d depicts the current-voltage (J - V) curves measured via forward and reverse bias sweep for the best-performance PSCs. The corresponding photovoltaic parameters under the optimized conditions with an active area of 0.09 cm², including of short-circuit current density (J_{sc}), open-circuit

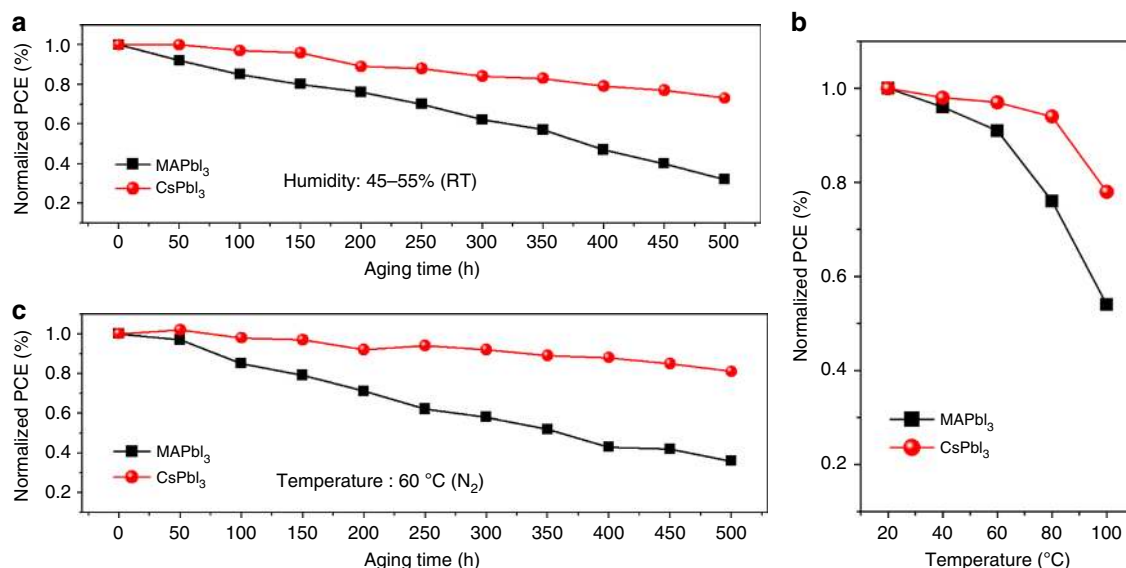


Fig. 5 Moisture and thermal stability investigation of perovskite solar cells based cubic CsPbI₃. **a** Efficiency evolution of the devices exposed in ambient air under relative humidity of 45–55% without any sealing. The measurements were carried every 50 h during 500 h. **b** Efficiency variation as a function of temperature from 20 to 100 °C. The PCEs were measured under nitrogen atmosphere after an equilibration time of 30 min at each temperature setting. **c** Efficiency evolution of the cells in a nitrogen atmosphere at 60 °C during 500 h

voltage (V_{oc}), fill factor (FF), and PCE values are summarized in the insert of Fig. 4d. The J_{sc} , V_{oc} , and FF for forward sweep of the device are 14.79 mA cm⁻², 1.08 V, and 65%, respectively, corresponding to a PCE of 10.38% under standard AM 1.5 G condition. With faint hysteresis, the solar device for reverse sweep exhibits a J_{sc} of 14.88 mA cm⁻², a V_{oc} of 1.11 V and a PCE of 10.74%, which are higher than those of previous reports on CsPbBr₃ and CsPbBr_{3-x}I_x (Supplementary Table 2)^{18,19,35}. Moreover, the stability of J_{sc} and PCE for both devices is shown in Supplementary Figure 19. The cubic CsPbI₃ device shows a stable output with a J_{sc} of 13.1 mA cm⁻² and a PCE of 10.0%. The corresponding incident photo-to-current efficiency (IPCE) spectrum in Fig. 4c for the best cell exhibits a broad plateau of over 60% between 350 and 700 nm. The integrated J_{sc} of 14.7 mA cm⁻² is in good agreement with the current density acquired from the current–voltage measurement. Intriguingly, compared with other inorganic PSCs^{18,19,35}, the CsPbI₃ based solar cell exhibits a much higher J_{sc} , which can be attributed to the extended visible-light-absorption range and extra-long carrier diffusion length for CsPbI₃, beneficial to more photoelectrons/hole generations and captures by corresponding transport layers. Moreover, the PVP covered on CsPbI₃ grains decreases surface defects and suppresses nonradiative recombination, significantly (Supplementary Figure 17). Figure 4e shows a histogram of average PCEs from all of the cubic CsPbI₃ PSCs fabricated under the same condition for the repeatability purpose. Over 70% of the devices exhibit over 8% PCE, and the average PCE summarized shows 8.50%, which is better than most current stable and efficient CsPbI₂Br perovskite cells (Supplementary Figure 20).

Moisture and thermal stability. The excellent stability of PSCs is an essential factor for the reproducibility and commercial application. To investigate the moisture and thermal stability under different conditions, the performance of inorganic cubic perovskite (CsPbI₃) PSCs with average PCE is comparatively measured with that of solar cells based on typical organic–inorganic hybrid perovskite (MAPbI₃). The ambient-humidity-stability test was conducted under ambient condition for 500 h without encapsulation (average humidity of 45–55% with temperature of

26 °C fixed). Fig. 5a shows the device moisture-stability as a function of aging time in terms of normalized power conversion efficiency (PCE). During 500 h, the cell of MAPbI₃ shows a dramatic drop with 70% efficiency loss with respect to the fresh solar cell. Comparatively, cubic CsPbI₃ based device exhibits a better moisture-stability with 75% retention after 500 h. Figure 5b shows the thermal-stability measurement of PSCs with cubic CsPbI₃ and MAPbI₃, which was conducted at different temperature ranging from 20 to 100 °C. It is clear that, with the increasing of temperature, the inorganic cubic perovskite exhibits more prominent thermal stability, showing over 90% efficiency retention even at 80 °C. It is worth noting that, as increasing the temperature to 100 °C, the devices of both CsPbI₃ and MAPbI₃ show obvious decay in PCE, which might result from the failure of the organic hole transport material. For further investigating the long-term thermal stability of the inorganic perovskite CsPbI₃ solar cell, we measured the device performance as stored at high temperature (60 °C) under normal sunlight exposure, which is shown in Fig. 5c. During 500 h measurement, the cubic CsPbI₃ based PSC shows a slight efficiency decay of only around 10%, demonstrating an outstanding superiority in thermal stability compared to MAPbI₃ based solar cell (70% efficiency loss). Notably, the thermal-stability efficiency test for inorganic perovskite exhibits a slower decay rate than the humidity stability. The result demonstrates that the CsPbI₃ inorganic perovskite possesses more outstanding stability, especially in thermal stability.

Discussion

In summary, we developed a surface passivation engineering for preparing long-term stable cubic phase CsPbI₃ films via a reproducible solution-chemistry process with the assistant of PVP. We proposed a plausible mechanism for the formation of stable cubic CsPbI₃ by investigating the surface chemical states of the perovskite crystals. The decreased surface tension can be obtained to stabilize CsPbI₃ grains in cubic phase even in micrometer scale, due to electron cloud density enhancement on the surface of CsPbI₃ originated from chemical bonding between acylamino in PVP and CsPbI₃. Furthermore, we found the

obtained cubic CsPbI₃ exhibits prominent photoelectronic properties with extra-long carrier lifetime of 338.7 ns and diffusion length of greater than 1.5 μm , up to an order of magnitude compared to the absorption depth. Based on this strategy, we have achieved the highest PCE of 10.74%, as well as excellent thermal/moisture stability in the fabricated inorganic PSCs. This result provides important progress towards the understanding of phase stability in the realization of large-scale preparations of efficient and stable inorganic PSCs.

Methods

Inorganic perovskite film preparation. A certain amount of PVP (Aladdin, K13-18) was first dissolved in mixed solvent with DMF (Aladdin, 99.9%) and DMSO (Aladdin, anhydrous) (1:1) and stirred for 30 min at room temperature. The CsPbI₃ precursor solution (0.8 M) was synthesized by dissolving stoichiometric CsI (Aladdin, 99.9%) and PbI₂ (Aladdin, 99.9%) in above solution, then, was stirred at 90 °C for 1 h on hot plate. The perovskite precursor solution was spin-coated on glass substrate or mesoporous TiO₂ film at 2500 rpm for 45 s and sintered at 300 °C for 5 min to form CsPbI₃ film. The other series of cesium lead halide perovskite films with different iodide/bromide proportions were synthesized by changing the percentage of PbI₂ and PbBr₂, and keeping other methods fixed.

Device fabrication. A compact TiO₂ layer (about 50 nm) was deposited on the FTO substrates (OPV Tech) which were ultrasonically washed and underwent oxygen plasma treatment by spin-coating a mildly acidic solution of titanium isopropoxide in ethanol (2000 rpm, 30 s), and annealed at 500 °C for 30 min. A 400–500 nm thick mesoporous TiO₂ film was coated on the compact layer via TiO₂ paste (2500 rpm, 45 s), next, heated for 30 min at 500 °C. Then, the CsPbI₃ active layer was deposited on mesoporous TiO₂ scaffold with 300 °C annealing treatment for 5 min. To increase the surface coverage of the inorganic perovskite, the substrates with TiO₂ coated were preheated at 150 °C. After cooling to room temperature, the substrates were immersed into IPA for 30 min to remove redundant PVP. Finally, an around 200 nm hole transport layer of spiro-OMeTAD (OPV Tech, 99.5%) was spin-coated at 2500 rpm for 30 s and a 50 nm gold counter electrode was prepared by thermal evaporation. The optical active layer and hole transport layer were fabricated in glove box.

Characterization. The XRD spectra of inorganic perovskite films were measured by Phillips Rigaku D/Max-kA X-ray diffractometer. The surface-section/cross-section morphologies of the perovskite films were characterized using field-emission scanning electron microscopy (FESEM, SU-70). The high-resolution transition electron microscope (HRTEM, Phillips, Tecnai 20U-Twin) was applied to analyze the structures and morphologies of the perovskite crystalline grains. The ultraviolet–visible absorption spectra of the perovskite films were recorded on the TU-1901 spectro-photometer. The FTIR spectra (NEXUS 670) were used to measure the surface functional group of the films. The liquid-state NMR were conducted by VNMRs 600. The XPS measurement was carried out using the Escalab 250Xi electron spectrometer via monochromatized Al K α radiation ($h\nu = 1486.7\text{ eV}$). The TRPL measurement were carried by FLS920 all functional fluorescence spectrometer (Edinburgh) with an excitation wavelength of 400 nm. The photovoltaic performances ($J-V$ curves) were analyzed by a solar simulator (Newport, Class 3 A, 94023 A) set an AM 1.5 G simulated sunlight (100 mW cm⁻²) equipped with a Keithley 2420, and the solar cells were measured using a metal aperture to define the active area to be around 0.09 cm². The IPCE was characterized using a power source (Newport 300 W xenon lamp, 66920) equipped with a monochromator (Newport Cornerstone 260) and a multimeter (Keithley 2400) at 100 mW cm⁻², AM 1.5 G illumination, and was corrected by a calibrated Si-reference cell (NREL).

Data availability. All data used in this study are available from the corresponding authors upon reasonable request.

Received: 24 September 2017 Accepted: 25 January 2018

Published online: 14 March 2018

References

- Stranks, S. D. et al. Electron-hole diffusion lengths exceeding 1 micrometer in an organometal trihalide perovskite absorber. *Science* **342**, 341–344 (2013).
- Lin, Q. et al. Electro-optics of perovskite solar cells. *Nat. Photonics* **9**, 106–112 (2015).
- Nie, W. et al. High-efficiency solution-processed perovskite solar cells with millimeter-scale grains. *Science* **347**, 522–525 (2015).
- Kim, H.-S. et al. Lead iodide perovskite sensitized all-solid-state submicron thin film mesoscopic solar cell with efficiency exceeding 9%. *Sci. Rep.* **2**, 591 (2012).
- Lee, M. M. et al. Efficient hybrid solar cells based on meso-superstructured organometal halide perovskites. *Science* **338**, 643–647 (2012).
- Burschka, J. et al. Sequential deposition as a route to high-performance perovskite-sensitized solar cells. *Nature* **499**, 316–319 (2013).
- Jeon, N. J. et al. Solvent engineering for high-performance inorganic–organic hybrid perovskite solar cells. *Nat. Mater.* **13**, 897–903 (2014).
- Jeon, N. J. et al. Compositional engineering of perovskite materials for high-performance solar cells. *Nature* **517**, 476–480 (2015).
- Wang, Z. et al. Stability of perovskite solar cells: a prospective on the substitution of the A cation and X anion. *Angew. Chem. Int. Ed.* **56**, 1190–1212 (2017).
- Kulbak, M., Cahen, D. & Hodes, G. How important is the organic part of lead halide perovskite photovoltaic cells? Efficient CsPbBr₃ cells. *J. Phys. Chem. Lett.* **6**, 2452–2456 (2015).
- Liang, J. et al. All-inorganic perovskite solar cells. *J. Am. Chem. Soc.* **138**, 15829–15832 (2016).
- Li, B. et al. PbCl₂-tuned inorganic cubic CsPbBr₃(Cl) perovskite solar cells with enhanced electron lifetime, diffusion length and photovoltaic performance. *J. Power Sources* **360**, 11–20 (2017).
- Kulbak, M. et al. Cesium enhances long-term stability of lead bromide perovskite-based solar cells. *J. Phys. Chem. Lett.* **7**, 167–172 (2016).
- Eperon, G. E. et al. Inorganic caesium lead iodide perovskite solar cells. *J. Mater. Chem. A* **3**, 19688–19695 (2015).
- Zhang, T. et al. Bication lead iodide 2D perovskite component to stabilize inorganic α -CsPbI₃ perovskite phase for high-efficiency solar cells. *Sci. Adv.* **3**, e1700841 (2017).
- Hu, Y. et al. Bismuth incorporation stabilized α -CsPbI₃ for fully inorganic perovskite solar cells. *ACS Energy Lett.* **2**, 2219–2227 (2017).
- Choi, H. et al. Cesium-doped methylammonium lead iodide perovskite light absorber for hybrid solar cells. *Nano Energy* **7**, 80–85 (2014).
- Sutton, R. J. et al. Bandgap-tunable cesium lead halide perovskites with high thermal stability for efficient solar cells. *Adv. Energy Mater.* **6**, 1502458 (2016).
- Ma, Q. et al. Hole transport layer free inorganic CsPbI₃ perovskite solar cell by dual source thermal evaporation. *Adv. Energy Mater.* **6**, 1502202 (2016).
- Chen, C.-Y. et al. All-vacuum-deposited stoichiometrically balanced inorganic cesium lead halide perovskite solar cells with stabilized efficiency exceeding 11%. *Adv. Mater.* **29**, 1605290 (2017).
- Beal, R. E. et al. Cesium lead halide perovskites with improved stability for tandem solar cells. *J. Phys. Chem. Lett.* **7**, 746–751 (2016).
- Li, X. et al. CsPbX₃ quantum dots for lighting and displays: room-temperature synthesis, photoluminescence superiorities, underlying origins and white light-emitting diodes. *Adv. Funct. Mater.* **26**, 2435–2445 (2016).
- Protesescu, L. et al. Nanocrystals of cesium lead halide perovskites (CsPbX₃, X=Cl, Br, and I): novel optoelectronic materials showing bright emission with wide color gamut. *Nano Lett.* **15**, 3692–3696 (2015).
- Li, B. et al. Graded heterojunction engineering for hole-conductor-free perovskite solar cells with high hole extraction efficiency and conductivity. *Adv. Mater.* **29**, 1701221 (2017).
- Swarnkar, A. et al. Quantum dot-induced phase stabilization of α -CsPbI₃ perovskite for high-efficiency photovoltaics. *Science* **354**, 92–95 (2016).
- Zhang, Z., Zhao, B. & Hu, L. PVP protective mechanism of ultrafine silver powder synthesized by chemical reduction processes. *J. Solid State Chem.* **121**, 105–110 (1996).
- Wang, H. et al. Mechanisms of PVP in the preparation of silver nanoparticles. *Mater. Chem. Phys.* **94**, 449–453 (2005).
- Lau, C. & Mi, Y. A study of blending and complexation of poly(acrylic acid)/poly(vinyl pyrrolidone). *Polymer* **43**, 823–829 (2002).
- Li, X. et al. Improved performance and stability of perovskite solar cells by crystal crosslinking with alkylphosphonic acid ω -ammonium chlorides. *Nat. Chem.* **7**, 703–711 (2015).
- Sesta, B. et al. ¹H NMR, surface tension, viscosity, and volume evidence of micelle-polymer hydrophobic interactions: LiPF₆-PVP system. *J. Phys. Chem. B* **101**, 198–204 (1997).
- Zhao, Y. et al. A polymer scaffold for self-healing perovskite solar cells. *Nat. Commun.* **7**, 10028 (2016).
- Yin, Q. et al. Micellization and aggregation properties of sodium perfluoropolyether carboxylate in aqueous solution. *J. Ind. Eng. Chem.* **42**, 63–68 (2016).
- Ummadisingu, A. et al. The effect of illumination on the formation of metal halide perovskite films. *Nature* **545**, 208–212 (2017).
- Kramer, D. Dependence of surface stress, surface energy and surface tension on potential and charge. *Phys. Chem. Chem. Phys.* **10**, 168–177 (2008).
- Nam, J. K. et al. Potassium incorporation for enhanced performance and stability of fully inorganic cesium lead halide perovskite solar cells. *Nano Lett.* **17**, 2028–2033 (2017).

Acknowledgements

We acknowledge support from the project supported by the State Key Program of National Natural Science of China (No.: 51532005), the National Nature Science Foundation of China (No.: 51472148, 51272137), and the Tai Shan Scholar Foundation of Shandong Province.

Author contributions

L.Y. initiated and directed the study. B.L. conceived the original research idea. B.L. and Y.Z. conducted most of the device fabrication and measurements. S.Z. contributed to the deposition of electron extraction layer. T.Y. contributed to the deposition of hole extraction layer. L.F. contributed to the structural characteristics. L.Z. provided the mechanism idea. The manuscript was co-written by L.Y. and B.L. All authors contributed to the discussion and revising of this manuscript.

Additional information

Supplementary Information accompanies this paper at <https://doi.org/10.1038/s41467-018-03169-0>.

Competing interests: The authors declare no competing interests.

Reprints and permission information is available online at <http://npg.nature.com/reprintsandpermissions/>

Publisher's note: Springer Nature remains neutral with regard to jurisdictional claims in published maps and institutional affiliations.



Open Access This article is licensed under a Creative Commons Attribution 4.0 International License, which permits use, sharing, adaptation, distribution and reproduction in any medium or format, as long as you give appropriate credit to the original author(s) and the source, provide a link to the Creative Commons license, and indicate if changes were made. The images or other third party material in this article are included in the article's Creative Commons license, unless indicated otherwise in a credit line to the material. If material is not included in the article's Creative Commons license and your intended use is not permitted by statutory regulation or exceeds the permitted use, you will need to obtain permission directly from the copyright holder. To view a copy of this license, visit <http://creativecommons.org/licenses/by/4.0/>.

© The Author(s) 2018